Electronic Supplementary Material (ESI) for ChemComm.

Supplementary Information

Acid etching followed by water soaking: a top-down strategy to induce highly reactive substrate for electrocatalysis

Experimental section

Chemicals

All reagents were of analytical grade and used without further purification. NiFe foam, Ni foam, NiMo foam, NiCo foam and NiZn foam (labeled as NFF, NF, NMoF, NCoF and NZnF, respectively) were purchased from Suzhou Jiashide Co., Ltd. Potassium hydroxide was purchased from Shanghai Meryer Chemical Technology Co. Ltd. Hydrochloric acid, ethanol, and acetone were purchased from Beijing Chemical Works. Milli-Q deionized water (resistance of 18.2 MΩ cm at 25 °C) were used for all experiments.

Fabrication of H^+&H_2O-NFF (or H^+&H_2O-24-NFF):

NFF (10×40 mm, 1 mm in thickness) was firstly cleaned ultrasonically in acetone, ethanol, and deionized water for 10 min, respectively, then dried in a blast drying oven at 60 °C in both steps prior to use. A piece of pretreated NFF was placed in a soaked in 3 M hydrochloric acid (HCl) for 1.5 h, then rinsed with deionized water (DIW) thoroughly and deionized water soaking for 24 h. After that, the treated NFF was rinsed with ethanol thoroughly. Subsequently, dried in a vacuum oven for 4 h at room temperature. Finally, the sample was named as H^+&H_2O-NFF or H^+&H_2O-24-NFF.

Fabrication of H^+-NFF and H_2O-NFF:

Control experiments were conducted for comparison. The pretreated NFF was placed in a soaked in 3 M HCl for 1.5 hours, then rinsed with DIW thoroughly, finally the sample was named as H^+-NFF. Similarly, the pretreated NFF was placed in deionized water soaking for 24 h, and the obtained sample was named as H_2O-NFF.

Fabrication of H^+&H_2O-6-NFF, H^+&H_2O-12-NFF and H^+&H_2O-36-NFF:

Similarly, H^+&H_2O-6-NFF, H^+&H_2O-12-NFF and H^+&H_2O-36-NFF were prepared via a same acid etching and water soaking route, except the time of soaking in deionized water is different (6, 12, and 36 represent different deionized water soaking time (unit: hour)). The obtained samples are named as H^+&H_2O-6-NFF, H^+&H_2O-12-NFF and H^+&H_2O-36-NFF, respectively.

Fabrication of H^+&H_2O-NF, H^+&H_2O-NMoF, H^+&H_2O-NCoF and H^+&H_2O-NZnF:

H^+&H_2O-NF, H^+&H_2O-NMoF, H^+&H_2O-NCoF and H^+&H_2O-NZnF were prepared using the same method as H^+&H_2O-NFF, except that the NFF substrate was replaced by NF, NMoF, NCoF and NZnF, respectively.

Materials Characterization:

The phase compositions of the catalysts were characterized by x-ray diffraction (XRD, Rigaku SmartLab, operated at 40 kV and 44 mA, parallel beam mode, λ=1.54 Å, step size 0.01 degree and scan rate 1 degree/min). Morphology observation and energy dispersive X-ray (EDS) spectrum analysis were conducted using a Zeiss Ultra 55 field emission scanning electron microscope (SEM). Transmission electron microscopy (TEM) characterization and selected area electron diffraction (SAED) pattern were obtained using an FEI Tecnai G2 20 microscope at 200 kV. X-ray photoelectron spectroscopy (XPS) analysis was performed on an ESCALab MKII spectrometer with Mg Ka X-ray as the excitation source. A laser micro-Raman spectrometer (Renishaw Invia) is using a visible laser (λ=514.5 nm) with an output laser power of 50 mW as the excitation wavelength at room temperature.

Electrochemical Measurement

The electrochemical measurements were carried out in a three-electrode system through the electrochemical workstation (CHI 760E). Hg/HgO was used as the reference electrode and Pt sheet (1 cm × 1 cm) as the counter electrode. OER performances were measured through performing linear sweep voltammetry (LSV, scan rate of 5 mV s^{-1}) in KOH (1.0 M) solution. All of the measured potentials (vs. Hg/HgO) were converted to the potentials against the reversible hydrogen electrode (RHE). All the obtained potentials vs Hg/HgO were converted to RHE according to Nernst equation $E_{RHE} = E_{Hg/HgO} + 0.0591\ pH + 0.098$. The long-term durability test was performed using chronopotentiometric measurements. EIS data were collected at the overpotential of 320 mV (vs. RHE) from 100 kHz to 0.01 Hz with an AC amplitude of 5 mV. All potentials presented were corrected against ohmic potential drop with 85% *iR* compensation. The ECSA was characterized according to a reported method.[1, 2] Specifically, CV (50, 60, 70, 80, and 100 mV s^{-1}) were collected in a narrow potential window of 0.724 V to 0.824 V (vs. RHE) where no faradaic reactions occurred. The capacitive currents of $\Delta J|J_a\text{-}J_c|/2$ are plotted with respect to the CV scan rates. The slope of the fitted line is the double layer capacitance (C_{dl}), which is proportional to the surface area of the electrode. The ECSA was calculated according to the following equation:

$$ECSA = \frac{C_{dl} \times A}{C_{ref}}$$

where A is the geometric area of the electrode (1 cm^2 in our case), C_{ref} is the referential areal capacitance of flat electrode (40 μF cm^{-2} is used as suggested by the ref.[3, 4]). In addition, HER performances were measured under the same conditions, except that the EIS data were collected at the overpotential of 100 mV (vs. RHE).

Similarly, the urea electrooxidation reaction (UOR) electrochemical measurements were also carried out in a three-electrode system through the electrochemical workstation (CHI 760E). Hg/HgO was used as the reference electrode and Pt mesh (1×1 cm) as the counter electrode. UOR performances were measured through performing linear sweep voltammetry (LSV, scan rate of 5 mV s^{-1}) in KOH (1.0 M) containing urea with the concentration of 0.5 M. All of the measured potentials (vs. Hg/HgO) were converted to the potentials against the reversible hydrogen electrode (RHE).

Supplementary Figures

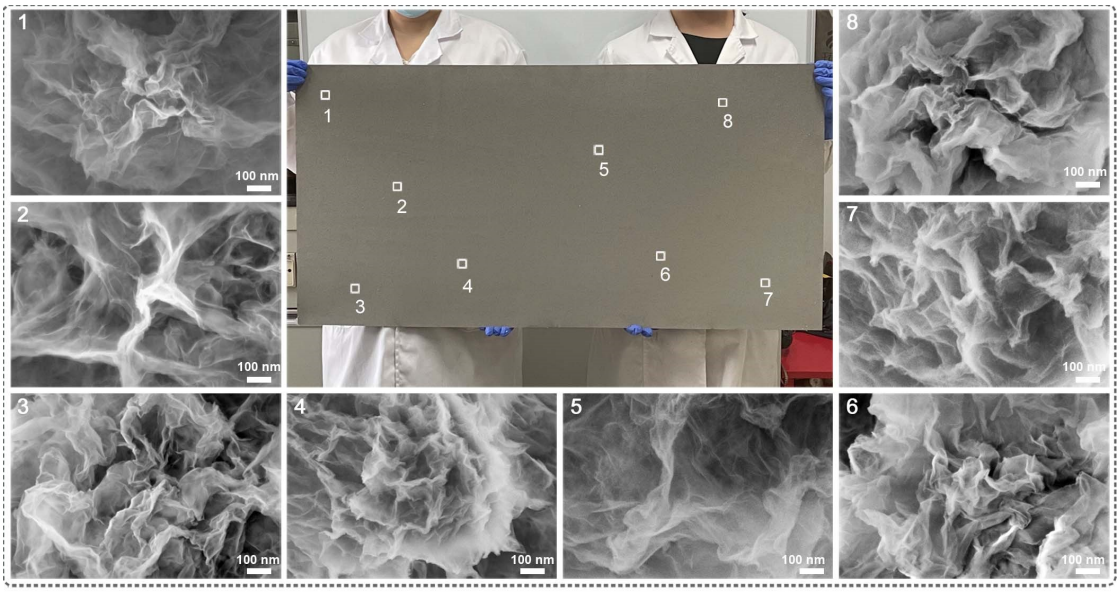

Fig. S1 (1-8). SEM image of large-scale H^+&H_2O-NFF prepared by the acid etching and water soaking, where the middle of is the corresponding optical photograph.

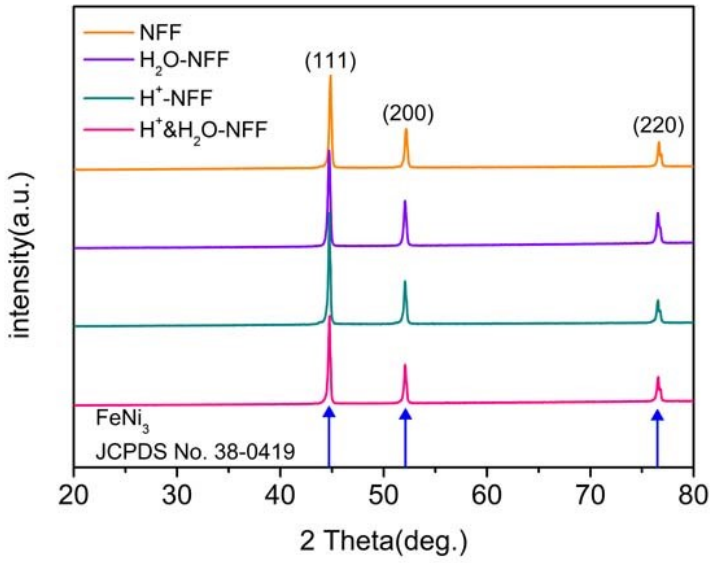

Fig. S2 XRD patterns of the pristine NFF, H_2O-NFF, H^+-NFF and H^+&H_2O-NFF.

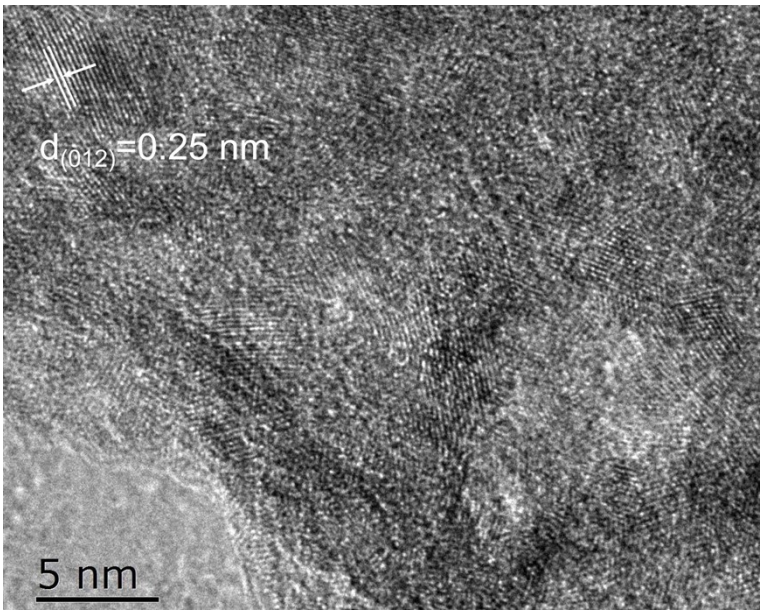

Fig. S3 High-resolution TEM image of the lattice fringes of the NiFe LDH (012) facet.

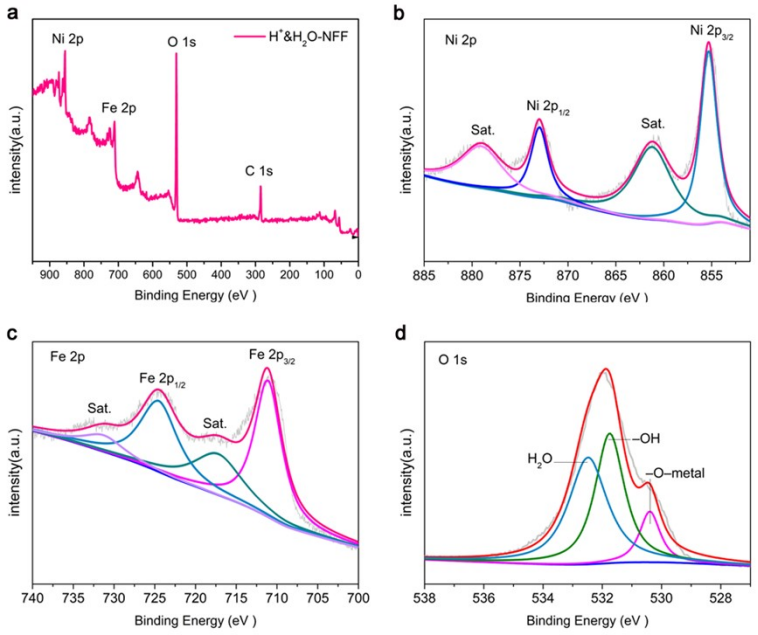

Fig. S4 (a) XPS survey spectrum of the H^+&H_2O-NFF. The high-resolution XPS spectra in the regions of (b) Ni 2p, (c) Fe 2p, and (d) O 1s for the NiFe-LDH on H^+&H_2O-NFF.

As depicted in Fig. S4a, the survey spectra confirm that the H^+&H_2O-NFF are composed of Fe, Ni, and O. In the Ni 2p high resolution spectrum of H^+&H_2O-NFF (Fig. S4b), the peaks at 855.3 and 872.9 eV correspond to the Ni^{2+}, accompanied by two prominent shakeup satellite peaks (861.2 and 879 eV)[5, 6]. The high resolution Fe 2p region in Fig. S3c exhibits four binding peaks at 711.1, 724.5, 717.2 and 731.2 eV belong to Fe $2p_{3/2}$, Fe $2p_{1/2}$ and two satellite peaks, suggesting the +3 oxidation state of the Fe species in H^+&H_2O-NFF (Fig. S4c)[5-7]. The three peaks at 530.4, 531.6 and 532.5 eV can be attributed to the contributions from the lattice of oxides, hydroxides and absorbed water, respectively (Fig. S4d)[5, 6, 8].

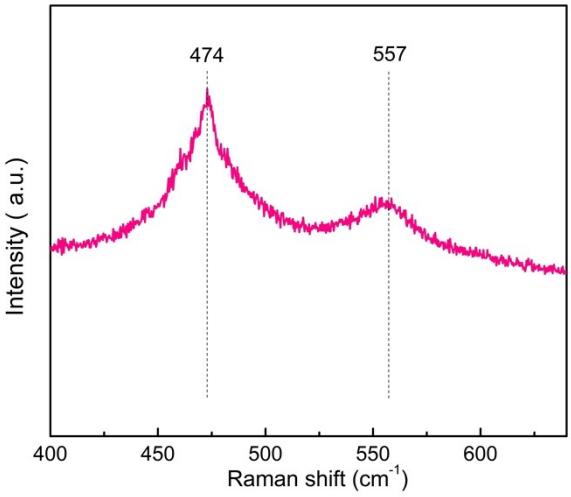

Fig. S5 Raman spectra of NiFe LDH.

Raman spectra were performed to investigate the composition of NiFe LDH. As shown in Fig. S5, two Raman peaks at 474 and 557 cm^{-1} are the characteristic peaks of NiFe LDH,[9] indicating the successful synthesis of NiFe LDH on the surface of H^+&H_2O-NFF.

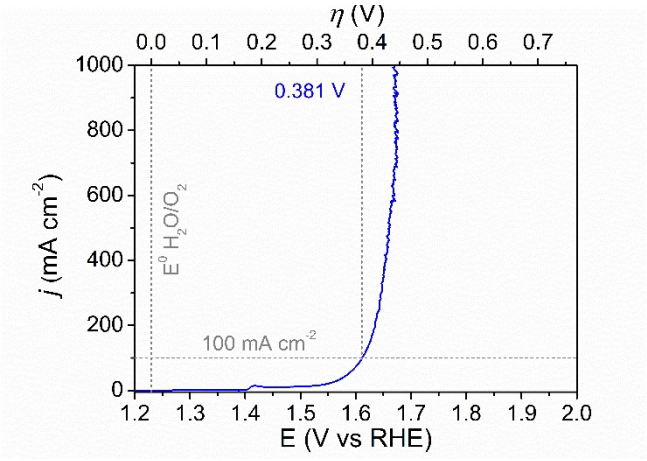

Fig. S6. OER polarization curve of RuO_2@NFF collected in 1.0 M KOH at a scan rate of 5 mV s^{-1}.

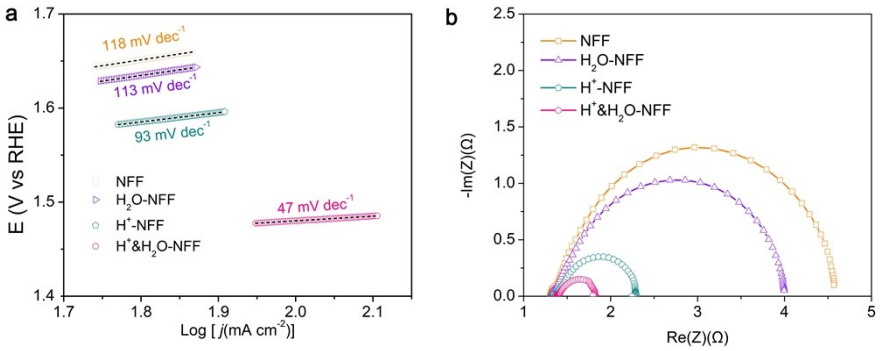

Fig. S7 (a) Tafel plots of NFF, H_2O-NFF, H^+-NFF, and H^+&H_2O-NFF. (b) The corresponding Nyquist plots at an overpotential of 370 mV.

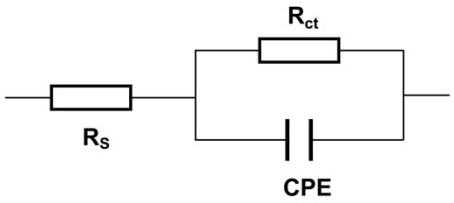

Fig. S8 Equivalent circuit used in the fitting of the impedance data of all samples. R_s: equivalent series resistance, R_{ct}: charge-transfer resistance, CPE: constant-phase element.

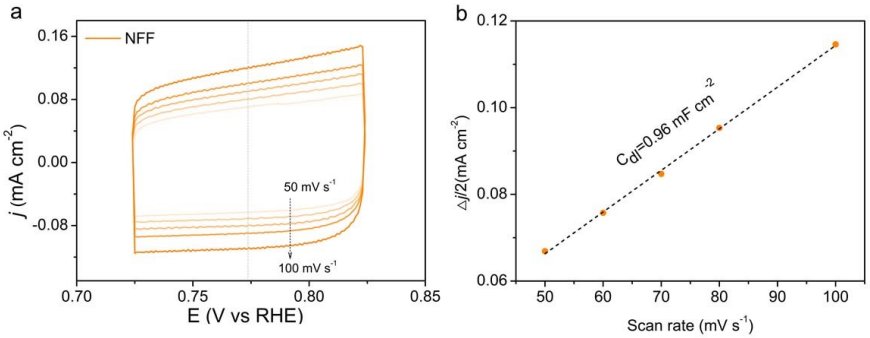

Fig. S9 Double-layer capacitance measurements for determining the ESCA of NFF from CV scans performed in 1 M KOH. (a) CV plots were measured in a non-Faradaic region of the voltammogram at the following scan rate: 50, 60, 70, 80, and 100 mV s^{-1}. (b) The corresponding linear fitting of the capacitive currents with respect to scan rates.

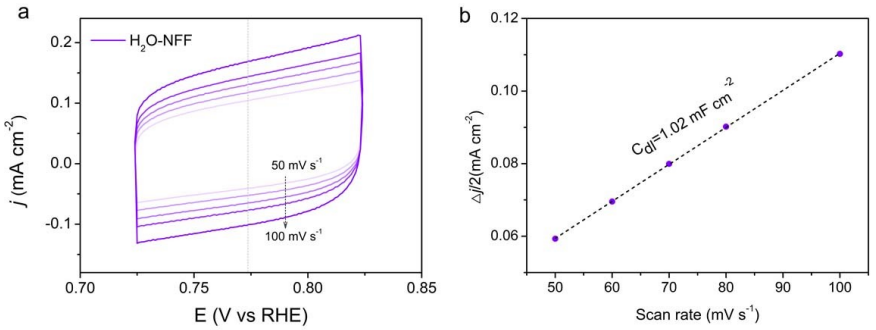

Fig. S10 H_2O-NFF of (a) Cyclic voltammograms at 50, 60, 70, 80, and 100 mV s^{-1}, and (b) the corresponding linear fitting of the capacitive currents with respect to scan rates. The calculated C_{dl} values are shown on the linear fitting of (b).

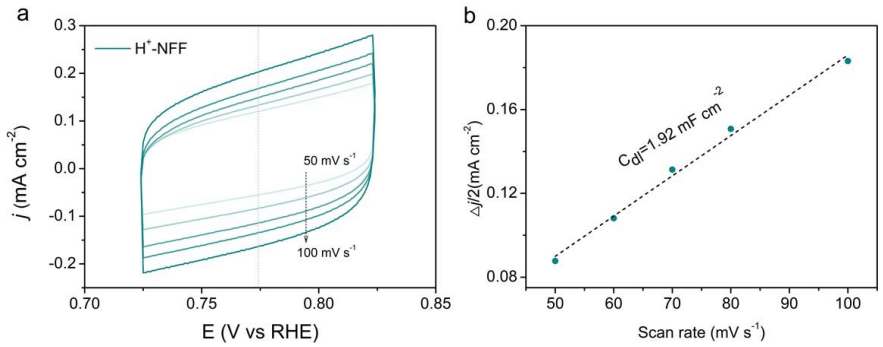

Fig. S11 H^+-NFF of (a) Cyclic voltammograms at 50, 60, 70, 80, and 100 mV s^{-1}, and (b) the corresponding linear fitting of the capacitive currents with respect to scan rates. The calculated C_{dl} values are shown on the linear fitting of (b).

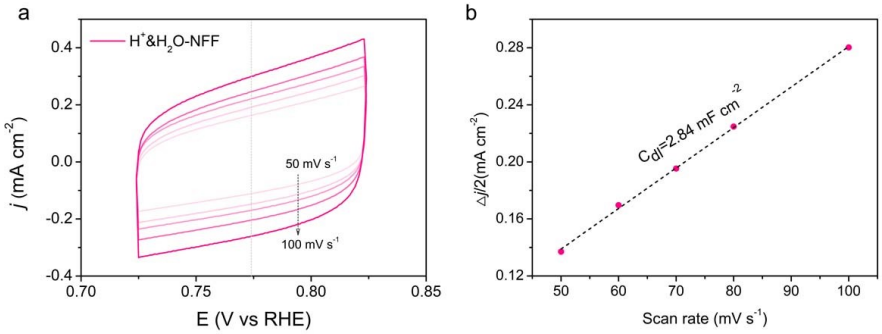

Fig. S12 H^+&H_2O-NFF of (a) Cyclic voltammograms at 50, 60, 70, 80, and 100 mV s^{-1}, and (b) the corresponding linear fitting of the capacitive currents with respect to scan rates. The calculated C_{dl} values are shown on the linear fitting of (b).

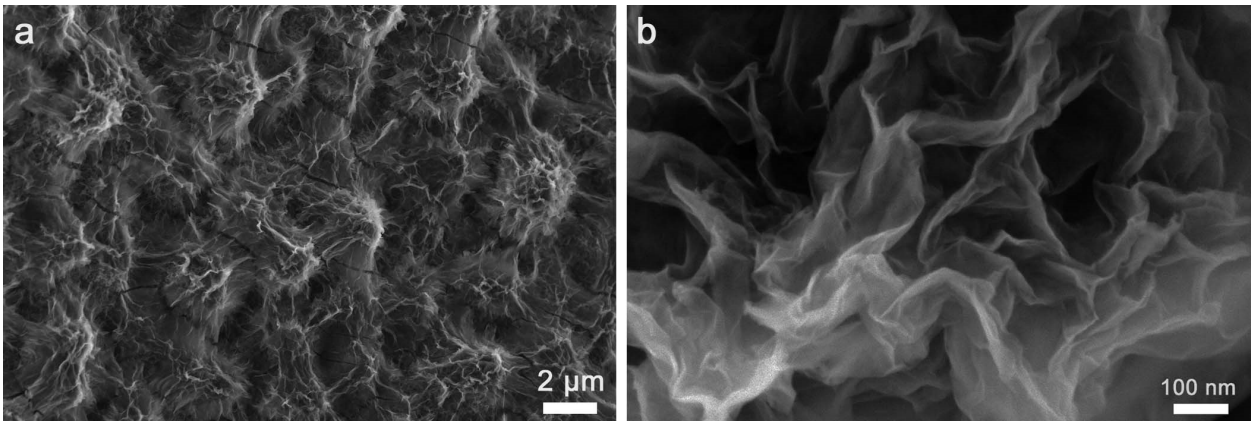

Fig. S13 Typical SEM image of H^+&H_2O-NFF after the chronopotentiometry measurement.

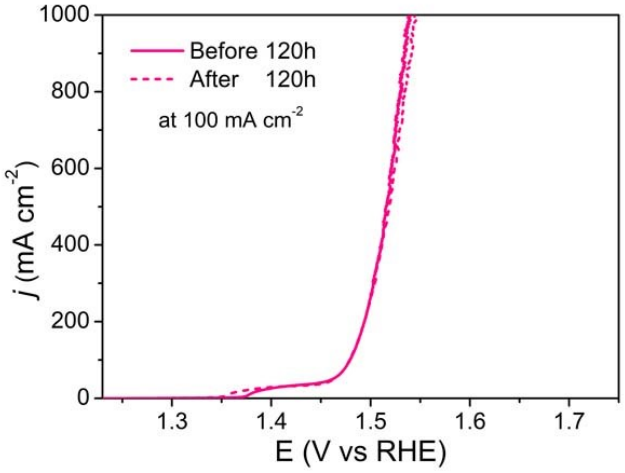

Fig. S14 OER polarization curves of H^+&H_2O-NFF before and after the OER test for 120 h.

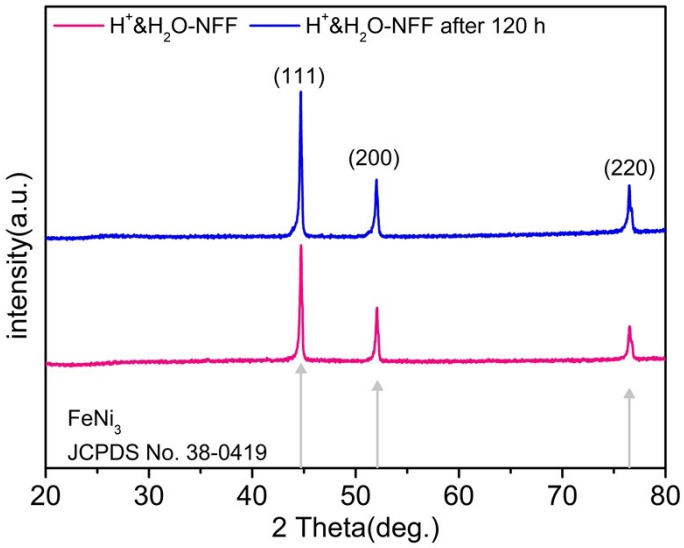

Fig. S15 XRD patterns of the H^+&H_2O-NFF and H^+&H_2O-NFF after 120 h.

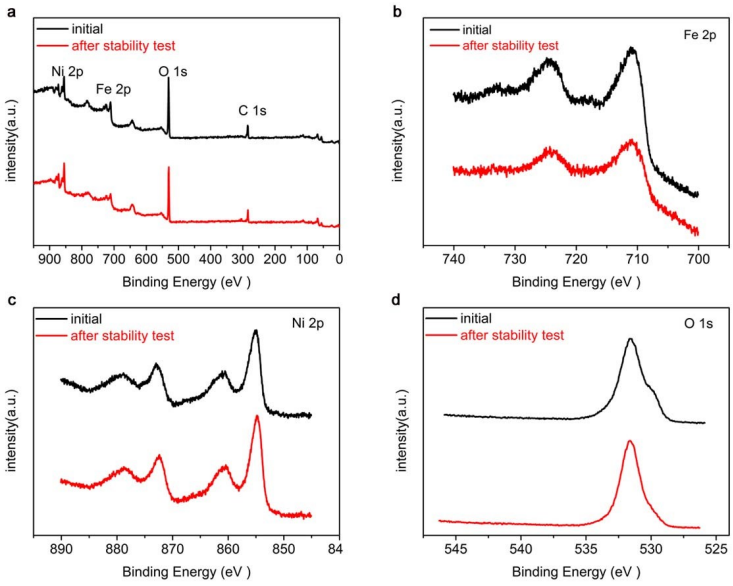

Fig. S16 XPS data of H^+&H_2O-NFF before and after long-term stability test. (a) XPS survey spectra and high resolution (b) Ni 2p, (c) Fe 2p, (d) O 1s spectra.

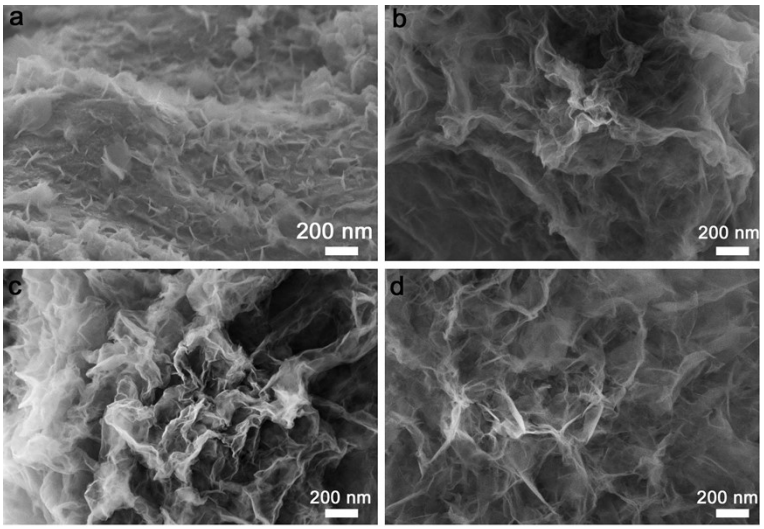

Fig. S17 SEM images of (a) H^+&H_2O-6-NFF, (b)H^+&H_2O-12-NFF, (c) H^+&H_2O-24-NFF and (d) H^+&H_2O-36-NFF.

Besides the acid etching obtained fresh NFF surface, the water soaking time is of course the crucial factor in determining NiFe LDH formation. A series of catalysts on NiFe foam were prepared by controlling the water soaking time to monitor the effects of H_2O activation on the performance of OER, UOR and HER. The images of SEM are shown in Fig. S17. The NiFe LDH nanosheets on the H^+&H_2O-6-NFF are relatively sparse, which would result in decreased active surface area. Moreover, the H^+&H_2O-12-NFF, H^+&H_2O-24-NFF and H^+&H_2O-36-NFF exhibit similar surface morphologies. With the extension of water soaking time, the nanosheets become larger and more closely interconnected. When it reaches 24 hours, the nanosheets are the most abundant. Nonetheless, opposite effects have been noted when the water soaking time goes to 36 hours. It is evident that H^+&H_2O-24-NFF show large and numerous nanosheet wrinkles, however, the nanosheets folds of H^+&H_2O-12-NFF and H^+&H_2O-36-NFF are not as rich as H^+&H_2O-24-NFF, which help to explain the excellent OER catalytic activity of H^+&H_2O-24-NFF in the four samples. Therefore, the key to achieving the numerous NiFe LDH lies in precisely regulating the water soaking time, achieving optimal H_2O activate effect.

The H^+&H_2O-NFF demonstrates a remarkably enhanced large-current–density catalytic activity and long-term stability for OER in alkaline solution, which is also utilized as a competent overall water splitting and urea oxidation trifunctional electrocatalyst. Comprehensive understanding of the catalytic performances of the electrocatalysts were achieved by studying their OER activities. The LSV curves of these experiments were operated at the scanning rate of 5 mV s^{-1} in 1.0 M KOH solution and were displayed in Fig. S18a. It can be seen that H^+&H_2O-24-NFF has the best excellent catalytic performance than the other four catalysts for OER. Based on the LSV curves of NFF, H^+&H_2O-6-NFF, H^+&H_2O-12-NFF, H^+&H_2O-24-NFF and H^+&H_2O-36-NFF, the corresponding Tafel slopes were derived to be 118, 109, 95, 54, and 47 mV dec^{-1}, and the H^+&H_2O-24-NFF displayed the lowest Tafel slope value (Fig. 18b), indicating the most rapid OER kinetics of H^+&H_2O-24-NFF. The EIS test was carried out in 1.0 M KOH electrolyte to study the electron transfer ability of the prepared electrocatalysts. The charge transfer resistances of NFF, H^+&H_2O-6-NFF, H^+&H_2O-12-NFF, H^+&H_2O-24-NFF and H^+&H_2O-36-NFF derived from the fitted equivalent circuit model were 3.27 Ω, 2.68 Ω, 0.96 Ω, 0.42 Ω and 2.42 Ω, respectively (Fig. S18c). In comparison with H^+&H_2O-6-NFF, H^+&H_2O-12-NFF, and H^+&H_2O-36-NFF, the R_{ct} value of H^+&H_2O-24-NFF was the smallest, which indicates that the fastest electron transfer rate at the interface of electrocatalyst electrolyte.[10] These conclusions prove that effective electron transfer kinetics of the H^+&H_2O-24-NFF. Besides, the HER performance of the as-prepared electrode and commercial Pt-mesh can be displayed in Fig. S18. The η of the H^+&H_2O-24-NFF electrocatalyst at current density of 100 mA cm^{-2} is 273 mV, which is significantly better than other samples and inferior to that of Pt-mesh at 122 mV (Fig. S19a). The Tafel slopes of NFF, H^+&H_2O-6-NFF, H^+&H_2O-12-NFF, H^+&H_2O-24-NFF, H^+&H_2O-36-NFF and Pt-mesh were 113.9 mV dec^{-1}, 112.7 mV dec^{-1} 104.1 mV dec^{-1}, 86.5 mV dec^{-1}, 109.8 mV dec^{-1} and 54.2 mV

dec^{-1}, respectively. Clearly, the Tafel slope of H^+&H_2O-24-NFF was much lower than those of the other catalysts except Pt-mesh (Fig. S19b), demonstrating the better HER kinetics of H^+&H_2O-24-NFF. Similarly, it can be seen from Fig. S19c that the charge transfer resistances of H^+&H_2O-24-NFF is the smallest compared with other samples, implying that H^+&H_2O-24-NFF possesses a rapid kinetic process.

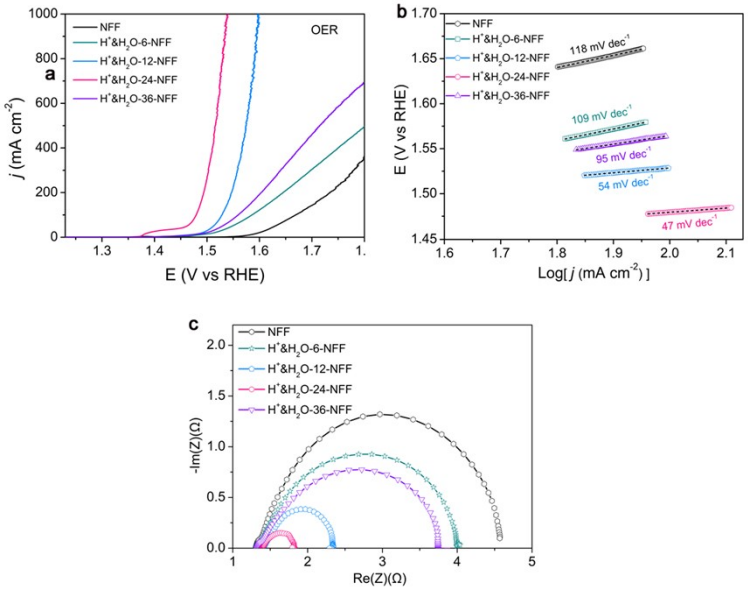

Fig. S18 NFF, H^+&H_2O-6-NFF, H^+&H_2O-12-NFF, H^+&H_2O-24-NFF and H^+&H_2O-36-NFF of (a) OER, (b) Tafel plots and (c) Nyquist plots.

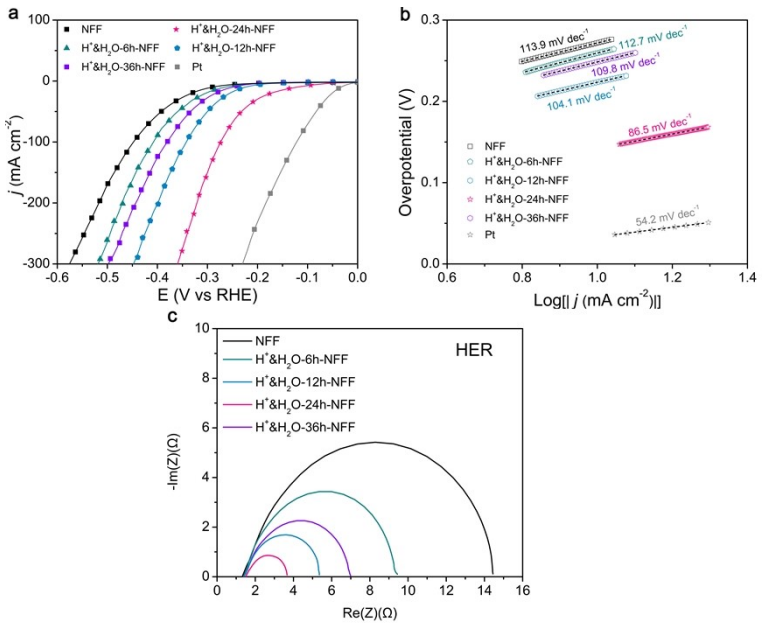

Fig. S19 NFF, H^+&H_2O-6-NFF, H^+&H_2O-12-NFF, H^+&H_2O-24-NFF H^+&H_2O-36-NFF and Pt of (a) HER, (b) Tafel plots and (c) Nyquist plots.

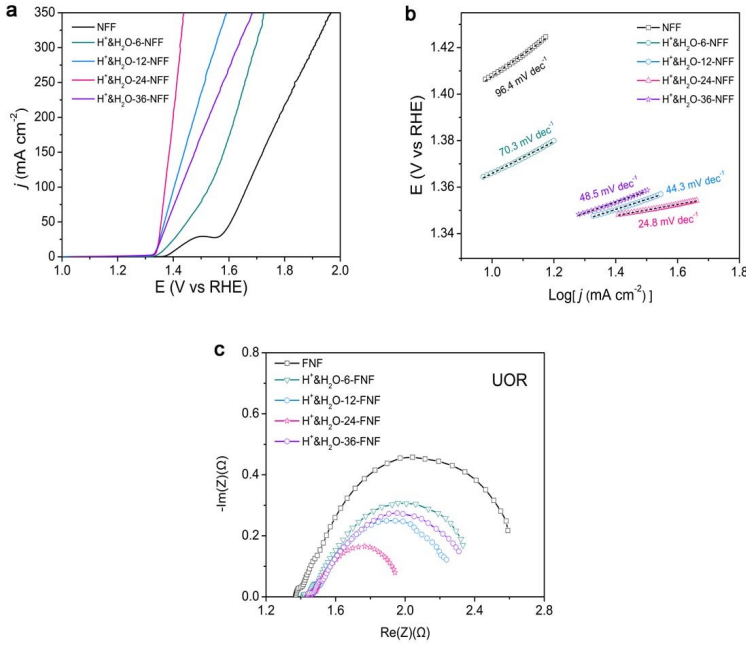

Fig. S20 NFF, H^+&H_2O-6-NFF, H^+&H_2O-12-NFF, H^+&H_2O-24-NFF and H^+&H_2O-36-NFF of (a) UOR, (b) Tafel plots and (c) Nyquist plots.

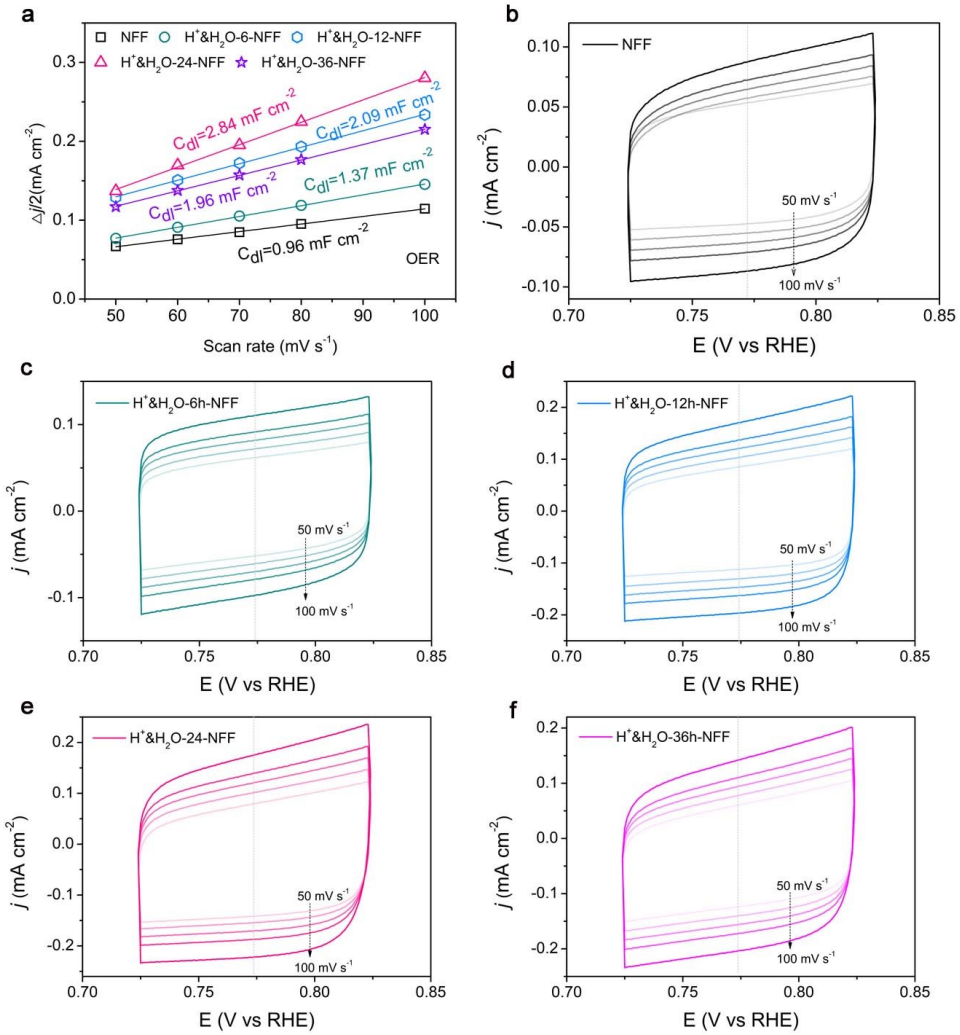

Fig. S21 NFF, H^+&H_2O-6-NFF, H^+&H_2O-12-NFF, H^+&H_2O-24-NFF and H^+&H_2O-36-NFF of (a) the corresponding linear fitting of the capacitive currents with respect to scan rates and the calculated C_{dl} values are shown on the linear fitting, and (b, c, d, e and f) Cyclic voltammograms at 50, 60, 70, 80, and 100 mV s^{-1}.

We used the double-layer capacitances (C_{dl}) to further analyze OER catalytic activities of the prepared electrocatalysts. In Fig. S21, the CV curves of different catalysts at disparate scanning rates were collected. In Fig. S21a, according to the above results, the corresponding C_{dl} values of NFF, H^+&H_2O-6-NFF, H^+&H_2O-12-NFF, H^+&H_2O-24-NFF, H^+&H_2O-36-NFF were counted by linear fitting with 0.96 mF cm^{-2}, 1.37 mF cm^{-2}, 2.09 mF cm^{-2}, 2.84 mF cm^{-2} and 1.96 mF cm^{-2}, respectively. Next, the electrochemical surface areas (ECSA) of the samples were obtained based

on the following equation ECSA = C_{dl} / Cs, in which ECSA was linear to C_{dl}, and Cs was a constant which had been released as 0.040 mF cm^{-2}.[3, 4] Accordingly, the ECSA values of the above electrocatalysts were calculated to be 24 cm^2, 34.25 cm^2 ,52.25 cm^2, 71 cm^2 and 49 cm^2, respectively, and the H^+&H_2O-24-NFF owned the highest value. This result supported that H^+&H_2O-24-NFF was able to provide more active sites than the other catalysts, thereby exhibited better catalytic activity in OER. The higher surface area of H^+&H_2O-24-NFF provides more accessible sites for electrochemical reactions. The surface area could be increased through a nanostructure strategy.[11]

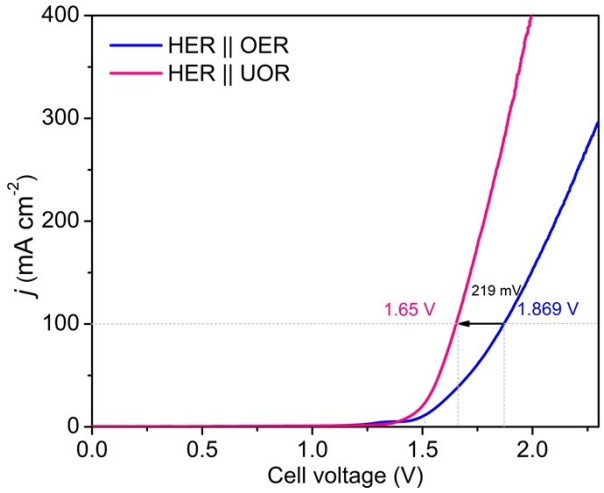

Fig. S22 Polarization curves of H^+&H_2O-NFF couple electrodes in HER||OER and HER||UOR coupled systems.

As OER is always suffering from high thermodynamic and slow reaction kinetics voltage, its application in the two-electrode system for producing H_2 is significantly restricted. Herein, urea oxidation reaction (UOR) might be a wise alternative due to its lower thermodynamic voltage. Then, we analyzed the UOR behavior of the catalysts using the LSV curves of the oxidation reaction. According to Fig. S20a, the activity of the catalysts for UOR followed the same law in OER. H^+&H_2O-24-NFF (η_{100} = 1.37 V) was better than H^+&H_2O-6-NFF (η_{100} = 1.528 V),

H^+&H_2O-12-NFF (η_{100} = 1.402 V) and H^+&H_2O-36-NFF (η_{100} = 1.428 V), and all of the initial voltages for UOR were lower than that of OER. Then, we tested the catalytic activity of the previously assembled H^+&H_2O-NFF ‖ H^+&H_2O-NFF electrode for whole urea electrolysis with 0.5 M urea. It can be seen that in the double electrode system containing urea, higher current density can be achieved with lower voltage, detailed in Fig. S22.

According to the LSV curves of the OER, HER and UOR, we proposed the overall water splitting and urea electrooxidation voltage, which is the voltage difference between OER, HER and UOR at the same current densities of 10, 20, 50, and 100 mA cm^{-2}. These voltages are almost the same as the voltages obtained from the H^+&H_2O-NFF ‖ H^+&H_2O-NFF LSV curves at the same current densities (Tab.S3). Moreover, the water splitting performance of the H^+&H_2O-NFF ‖ H^+&H_2O-NFF was compared with that commercial IrO_2 anode and Pt-mesh cathode device (denoted as Pt-Mesh//IrO_2-CC).[12] The voltage of the Pt-Mesh//IrO_2-CC electrolyzer LSV curves at the current densities of 10, 20, and 50 mA cm^{-2} to be 1.84, 1.94, and 2.18 V, respectively. Therefore, it is obvious that the H^+&H_2O-NFF ‖ H^+&H_2O-NFF electrolyzer displayed continuous lower voltage than the Pt-Mesh//IrO_2-CC, whether in water splitting or urea oxidation (Tab.S3). The H^+&H_2O-NFF ‖ H^+&H_2O-NFF electrolyzer is also characterized with smaller LSV slope along high current density and voltage, further confirming a favorable kinetics in the *in situ* self-supportive electrolyzer.

Fig. S23 High-magnification SEM images of 3D flower-like structures of (1) H^+&H_2O-NF, (2) H^+&H_2O-NZnF, (3) H^+&H_2O-NCoF, (4) H^+&H_2O-NMoF.

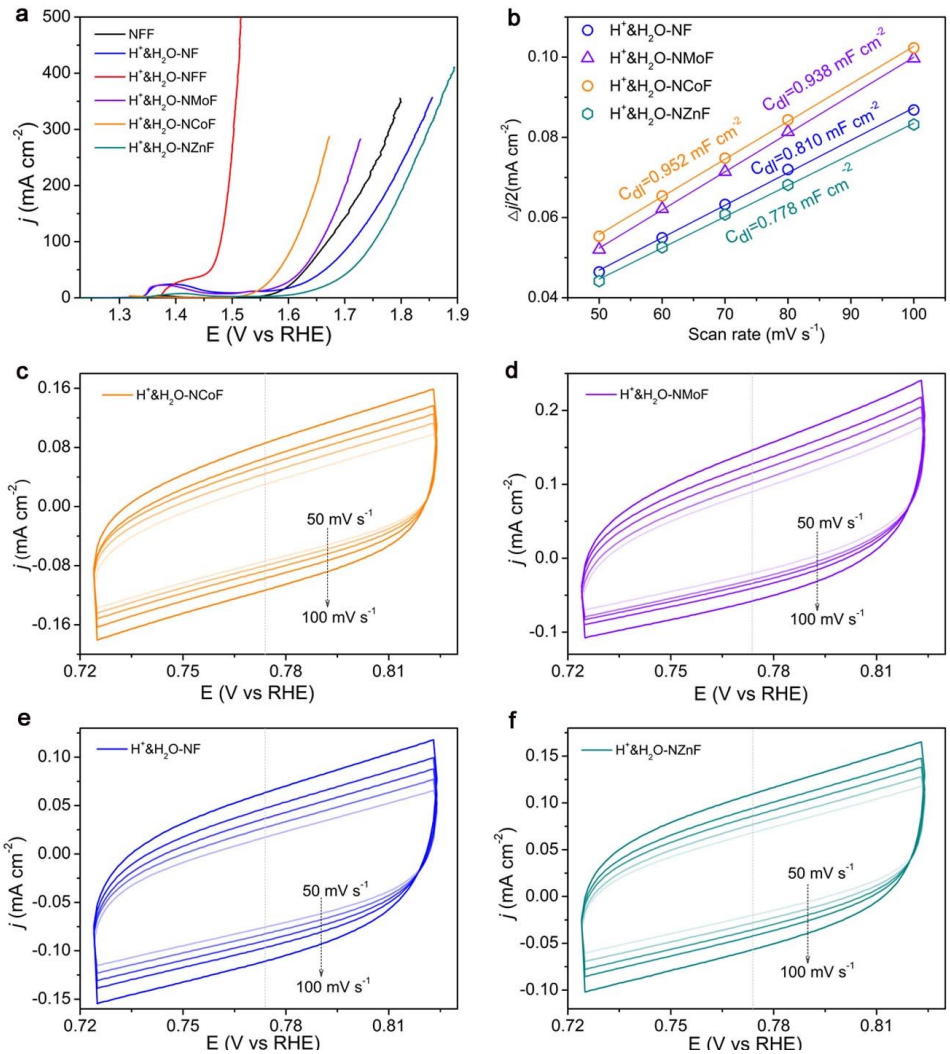

Fig. S24 (a) OER polarization curves of NFF, H^+&H_2O-NF, H^+&H_2O-NMoF, H^+&H_2O-NCoF, H^+&H_2O-NZnF and H^+&H_2O-NFF, and H^+&H_2O-NF, H^+&H_2O-NMoF, H^+&H_2O-NCoF, H^+&H_2O-NZnF of (b) the corresponding linear fitting of the capacitive currents with respect to scan rates and the calculated C_{dl} values are shown on the linear fitting, and (c, d, e and f) Cyclic voltammograms at 50, 60, 70, 80, and 100 mV s^{-1}.

The electrochemical experiments were carried out to evaluate the performance of these four electrocatalysts for OER. As shown in Fig. S24a, the H^+&H_2O-NZnF exhibits the worst OER activity with an overpotential of 521 mV at 100 mA cm^{-2}, which is much higher than 272 mV for H^+&H_2O-NFF. Obviously, the OER performance of these four electrocatalysts is much worse than

that of H^+&H_2O-NFF. This suggests that the high activity of H^+&H_2O-NFF originates from the synergistic effect between Ni and Fe elements, which is recognized in this field.[13]

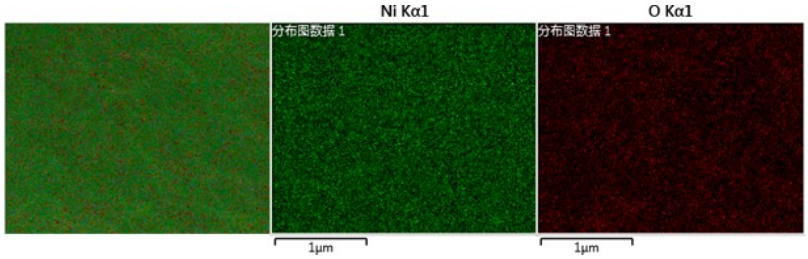

Fig. S25. the H^+&H_2O-NF EDS elemental mapping images of Ni and O.

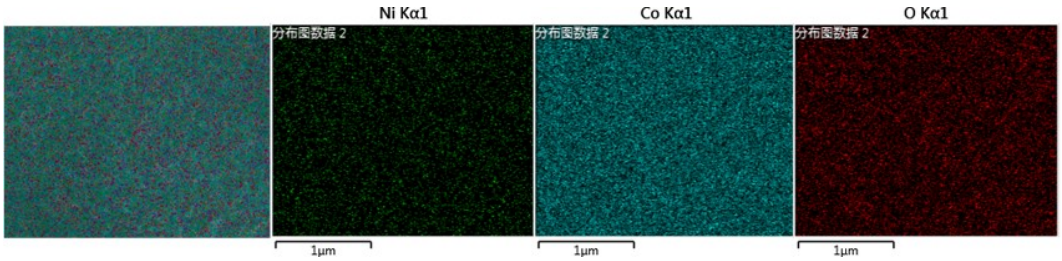

Fig. S26. the H^+&H_2O-NCoF EDS elemental mapping images of Ni, Co, and O.

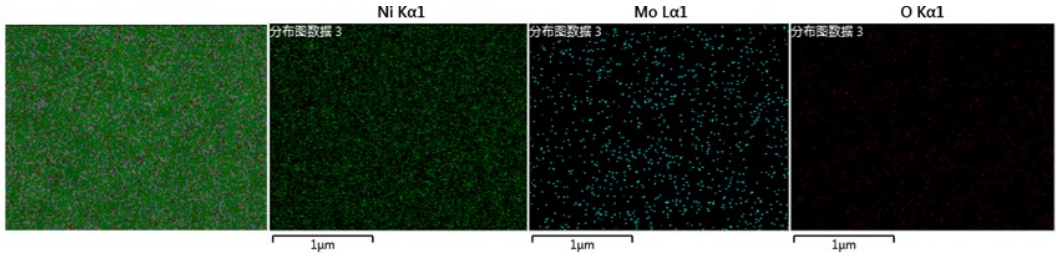

Fig. S27. the H^+&H_2O-NMoF EDS elemental mapping images of Ni, Mo, and O.

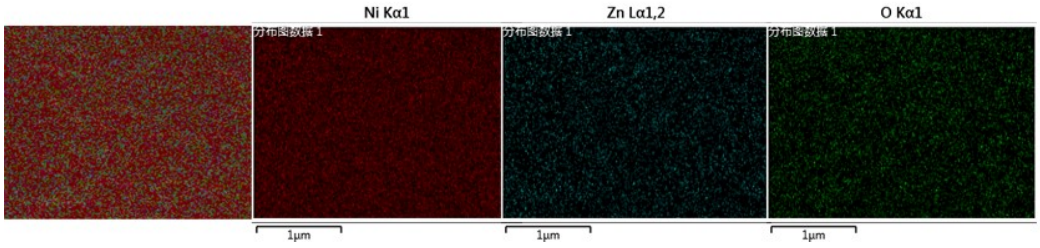

Fig. S28. the H^+&H_2O-NZnF EDS elemental mapping images of Ni, Zn, and O.

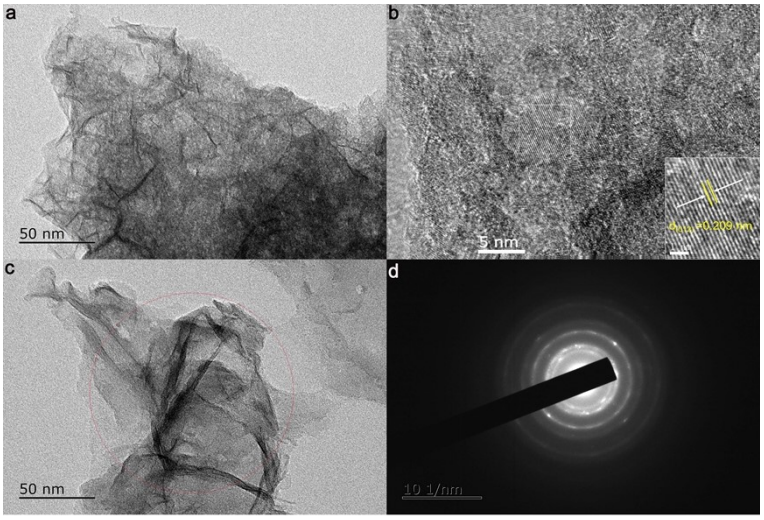

Fig. S29 (a)TEM image of NiMo LDH at low magnification. (b) HRTEM images of NiMo LDH and corresponding enlarged parts of the square region. (c-d) TEM and corresponding SAED pattern.

To characterize the surface nanosheets, the H^+&H_2O-NMoF was dispersed in ethanol solution by ultrasonic vibration and then collected for TEM observation. The nearly transparent nanosheets suggest that NiMo-LDH has ultrathin features (Fig. S29a). The lattice spacing of 0.209 nm was consistent with the (331) plane of the NiMo alloy (Fig. S29b).[14] The TEM images in Fig. S28c and corresponding SAED pattern (Fig. S29d) of NiMo LDH nanosheets exhibits that the diffuse rings with circular diffraction spots of the sample further verified the amorphous nature with numerous dispersed nanocrystals.[15]

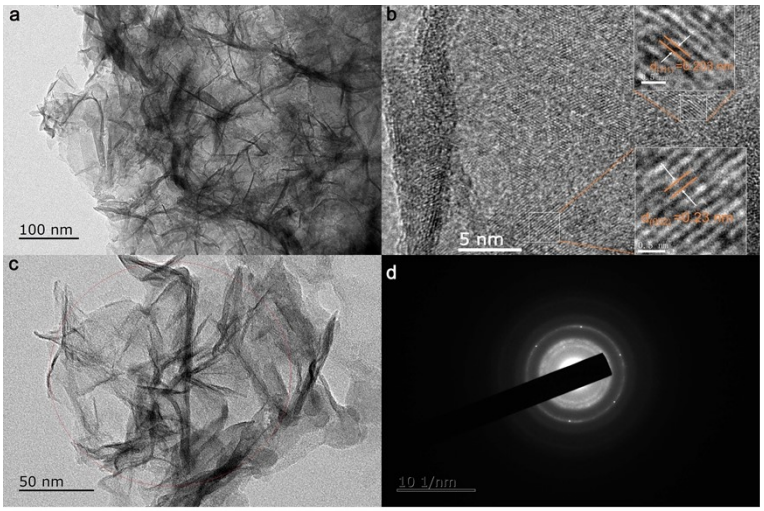

Fig. S30 (a)TEM and (b) HRTEM images of Ni and $Ni(OH)_2$ nanosheets and corresponding enlarged parts of the square regions. (c-d) TEM and corresponding SAED pattern.

From Fig. S30a, we can see the ultra-thin structure of nanosheets. The lattice fringes from different regions had a spacing of 0.203 and 0.23 nm (Fig. S30b), which could be ascribed to the (111) and (002) crystal planes of Ni and $Ni(OH)_2$, respectively.[16, 17]

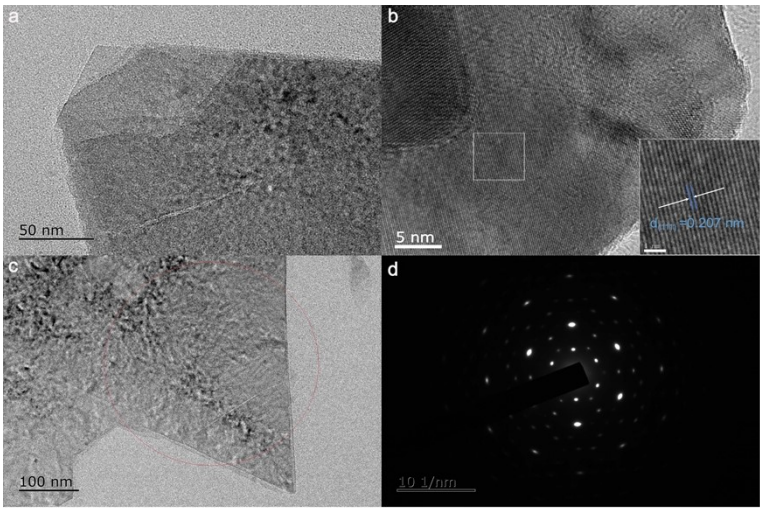

Fig. S31 (a)TEM image of NiCo LDH at low magnification. (b) HRTEM images of NiCo LDH and corresponding enlarged parts of the square region. (c-d) TEM and corresponding SAED pattern.

The structural and morphological information of H^+&H_2O-NCoF sample was further studied by TEM. The nearly transparent nanosheets suggest that NiMo-LDH has ultrathin features (Fig. S31a). The lattice spacing of 0.207 nm well related to the (107) plane of NiCo-LDH (Fig. S31b).[18] It is noted that , from the TEM images in Fig. S30c and corresponding SAED pattern (Fig. S31d) of NiCo LDH nanosheets can be seen the clear diffraction point , which can prove that the sample has crystal crystalline nature.

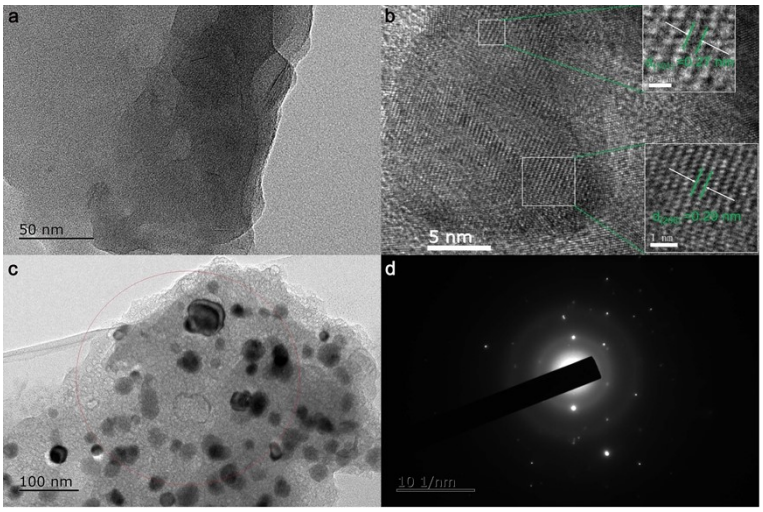

Fig. S32 (a)TEM image of NiZn LDH at low magnification. (b) HRTEM images of NiZn LDH and corresponding enlarged parts of the square regions. (c-d) TEM and corresponding SAED pattern.

The detailed information on sample structure in Fig. S32, different kinds of lattice fringes could be identified, as marked by squares. The lattice fringes from different regions had a spacing of 0.27 and 0.29 nm (Fig. S32b), which could be ascribed to the (101) and (206) crystal planes of NiZn LDH and $Zn(OH)_2$, respectively.[15, 19] It can be seen from Fig. S32c and Fig. S32d that the sample has crystalline and amorphous properties.

Supplementary Tables

Tab. S1. The radius (R) of the of the diffraction rings and the d-space between crystal plane*.

R_x	Length (unit: 1/nm)	d (unit: nm)	*hkl*
R_1	3.84	0.260	012
R_2	6.49	0.154	110
R_3	7.57	0.132	119

*note:1) d is the distance between crystal planes and it equals to 1/R.

2) The ***hkl*** values are assigned by pairing with the standard database, and it has been found they match well with the PDF# 40-0215 data corresponding to the structure of Iron Nickel Carbonate Hydroxide Hydrate crystals.

Tab. S2 OER performances of H^+&H_2O-NFF and other reported electrocatalysts (*j*: current density; η: overpotential).

catalysts	η (mV) @*j*=−100 mA cm^{-2}	Reference
H^+&H_2O-NFF	249	This work
FeNi-PPy HNSs	273	Appl. Catal. B **2020**, 274
N-NiFeOOH	278	ACS Appl. Mater. Interfaces **2018**, 10, 8786−8796
$Fe_{0.9}Ni_{2.1}S_2$ @ NF	252	Adv.EnergyMater.**2020**,10,2001963
sd-NFF	310	Chem. Commun., **2020**,56, 12399-12402
Ta-NiFe LDH	280	Chem. Eng. J. **2021**, 403, 126297
$Ni_{0.8}Fe_{0.2}$-m/t-$Se_{0.02}$-LDH	278	Nanoscale **2019**, 11
NiMoFeO@NC	290	Matter **2020**, 3, 2124
Ni:FeOOH/NGF	270	ACS Catal. **2019**, 9, 5025
S-(Ni,Fe)OOH	281	Energy Environ. Sci. **2020**, 13, 3439
Ni(Fe)OOH–FeSx	310	Nat. Commun. **2020**, 11, 1
FeCoNiOOH	330	Adv. Energy Mater. **2019**, 9, 1901312
NiFeOx/NiFeOOH	280	ACS Appl. Mater. Interfaces **2018**, 10, 8786−8796
NiFe(OH)x/FeS/IF	~251	Adv. Funct. Mater. **2019**, 1902180
γ-FeOOH/NF	320	Adv. Mater. **2021**, 2005587
FeNi@FeNiB-700	399	J. Mater. Chem. A, **2019**,7, 19554-19564
(Fe-Ni)Cox−OH/Ni_3S_2	280	Appl. Catal. B **2020**, 263, 118338.
$Ni_{1.5}$Sn@triMPO_4	330	Angew. Chem. Int. Ed.**2020**,14210
P-Ni_3S_2/$CoFe_2O_4$/NF	~270	J.Colloid and Interface Science ,**2021**,581,774-782
NiFe/NFF	253	Adv. Funct. Mater. 2018, 29, 1807418

Tab. S3 Values of equivalent circuit elements based on EIS analysis of different electrodes.

Eletrodes	R_s (Ω)	R_{ct} (Ω)
NFF	1.30	3.27
H_2O-NFF	1.31	2.69
H^+-NFF	1.34	0.96
H^+&H_2O-NFF	1.38	0.42

Tab. S4 Different current density(j) of overpotential (η) or voltage for H^+&H_2O-NFF.

η/voltage (V)	j =10 mA cm^{-2}	j =20 mA cm^{-2}	j =50 mA cm^{-2}	j =100 mA cm^{-2}
HER	0.121	0.171	0.232	0.273
OER	1.377	1.388	1.693	1.479
UOR	1.34	1.346	1.356	1.37
water electrolysis	1.499	1.568	1.699	1.869
urea electrolysis	1.462	1.519	1.59	1.667

Tab. S5 Comparison of the overall urea oxidation performance of the H^+&H_2O-NFF electrocatalyst and recently reported catalysts.

catalysts	Electrolyte	Voltage (V) @j=10 mA cm^{-2}	Reference
H^+&H_2O-NFF|| H^+&H_2O-NFF	1 M KOH +0.5M urea	1.462	This work
NiFeCo LDH/NF|| NiFeCo LDH/NF	1 M KOH +0.33M urea	1.49	20
Ni $(OH)_2$-NMs|| Ni $(OH)_2$-NMs	1 M KOH +0.33M urea	1.48	21
Pt/C/NF||IrO_2/C/NF	1 M KOH +0.5M urea	1.46	22
Ni_2P/Fe_2P/NF|| Ni_2P/Fe_2P/NF	1 M KOH +0.5M urea	1.47	23
HC-NiMoS/Ti|| HC-NiMoS/Ti	1 M KOH +0.5M urea	1.59	24
CoMn/$CoMn_2O_4$|| CoMn/$CoMn_2O_4$	1 M KOH +0.5M urea	1.51	25
NCS/CC1:2|| NCS/CC 1:2	1 M KOH +0.33M urea	1.52	26
NiFe/N–C||Pt	1 M KOH +1 M urea	1.5	27
Ni@C-25|| Ni@C-250	1 M KOH +0.5M urea	1.46	28

References

1. J. Kibsgaard, Z. Chen, B. N. Reinecke and T. F. Jaramillo, *Nat Mater*, 2012, **11**, 963-969.
2. J. Kibsgaard and T. F. Jaramillo, *Angew Chem Int Ed Engl*, 2014, **53**, 14433-14437.
3. J. D. Benck, Z. Chen, L. Y. Kuritzky, A. J. Forman and T. F. Jaramillo, *ACS Catalysis*, 2012, **2**, 1916-1923.
4. Q. Zhou, J. Pu, X. Sun, C. Zhu, J. Li, J. Wang, S. Chang and H. Zhang, *Journal of Materials Chemistry A*, 2017, **5**, 14873-14880.
5. D. Li, Z. Pan, H. Tao, J. Li, W. Gu, B. Li, C. Zhong, Q. Jiang, C. Ye and Q. Zhou, *Chem Commun (Camb)*, 2020, **56**, 12399-12402.
6. J. Wang, X. Teng, Y. Niu, L. Guo, J. Kong, X. He and Z. Chen, *RSC Adv*, 2019, **9**, 21679-21684.
7. H. Yang, C. Wang, Y. Zhang and Q. Wang, *Science China Materials*, 2018, **62**, 681-689.
8. G. Dong, M. Fang, J. Zhang, R. Wei, L. Shu, X. Liang, S. Yip, F. Wang, L. Guan, Z. Zheng and J. C. Ho, *Journal of Materials Chemistry A*, 2017, **5**, 11009-11015.
9. N. S. Gultom, H. Abdullah, C.-N. Hsu and D.-H. Kuo, *Chemical Engineering Journal*, 2021, **419**.
10. Q. Li, W. Zhang, J. Shen, X. Zhang, Z. Liu and J. Liu, *Journal of Alloys and Compounds*, 2022, **902**.
11. G. Chen, Y. Zhu, H. M. Chen, Z. Hu, S. F. Hung, N. Ma, J. Dai, H. J. Lin, C. T. Chen, W. Zhou and Z. Shao, *Adv Mater*, 2019, **31**, e1900883.
12. M. S. Balogun, W. Qiu, Y. Huang, H. Yang, R. Xu, W. Zhao, G. R. Li, H. Ji and Y. Tong, *Adv Mater*, 2017, **29**.
13. S. Niu, W. J. Jiang, Z. Wei, T. Tang, J. Ma, J. S. Hu and L. J. Wan, *J Am Chem Soc*, 2019, **141**, 7005-7013.
14. M. Fang, W. Gao, G. Dong, Z. Xia, S. Yip, Y. Qin, Y. Qu and J. C. Ho, *Nano Energy*, 2016, **27**, 247-254.
15. Q. Zhou, C. Xu, Y. Li, X. Xie, H. Liu and S. Yan, *Science China Materials*, 2021, **65**, 1207-1216.
16. Y. Tang, Q. Liu, L. Dong, H. B. Wu and X.-Y. Yu, *Applied Catalysis B: Environmental*, 2020, **266**.
17. S. Hu, H. Wu, C. Feng and Y. Ding, *International Journal of Hydrogen Energy*, 2020, **45**, 21040-21050.
18. F. Zhu, W. Liu, Y. Liu and W. Shi, *Chemical Engineering Journal*, 2020, **383**.
19. Y. Gong, J. Huang, L. Cao, K. Kajiyoshi, D. Yang, Y. Feng, L. Kou and L. Feng, *Dalton Trans*, 2020, **49**, 1325-1333.
20. P. Babar, A. Lokhande, V. Karade, B. Pawar, M. G. Gang, S. Pawar and J. H. Kim, *ACS Sustainable Chemistry & Engineering*, 2019, **7**, 10035-10043.
21. Y. Ding, Y. Li, Y. Xue, B. Miao, S. Li, Y. Jiang, X. Liu and Y. Chen, *Nanoscale*, 2019, **11**, 1058-1064.
22. Q. Xu, T. Yu, J. Chen, G. Qian, H. Song, L. Luo, Y. Chen, T. Liu, Y. Wang and S. Yin, *ACS Appl Mater Interfaces*, 2021, **13**, 16355-16363.
23. L. Yan, Y. Sun, E. Hu, J. Ning, Y. Zhong, Z. Zhang and Y. Hu, *J Colloid Interface Sci*, 2019, **541**, 279-286.
24. X. Wang, J. Wang, X. Sun, S. Wei, L. Cui, W. Yang and J. Liu, *Nano Research*, 2017, **11**, 988-996.

25. C. Wang, H. Lu, Z. Mao, C. Yan, G. Shen and X. Wang, *Advanced Functional Materials*, 2020, **30**.
26. P. Hao, W. Zhu, L. Li, J. Tian, J. Xie, F. Lei, G. Cui, Y. Zhang and B. Tang, *Electrochimica Acta*, 2020, **338**.
27. J. Zhang, F. Xing, H. Zhang and Y. Huang, *Dalton Trans*, 2020, **49**, 13962-13969.
28. J. Wang, Z. Zhao, C. Shen, H. Liu, X. Pang, M. Gao, J. Mu, F. Cao and G. Li, *Catalysis Science & Technology*, 2021, **11**, 2480-2490.